THE ASTROPHYSICAL JOURNAL, 498:763–772, 1998 May 10

ASTROPHYSICAL MASER RADIATION FROM A TURBULENT MEDIUM: APPLICATION TO 25 GHz METHANOL MASERS

A. M. SOBOLEV,[1,2] B. K. WALLIN,[2] AND W. D. WATSON[2]

Received 1997 July 30; accepted 1997 December 23

ABSTRACT

Spectral and spatial distributions are calculated for astrophysical maser radiation that emerges from a turbulent medium. Turbulent-velocity fields are created by sampling from Kolmogorov-like distributions. The maps of maser emission created in a turbulent medium appear as if the emission results from a collection of isolated clumps moving with different velocities, even though the physical quantities (other than velocity) are constant within the medium. A detailed comparison is made with observational data about the 25 GHz methanol masers in OMC-1. There is evidence that key simplifications for the calculations—unsaturated masing and uniform excitation—are applicable for these masers. For the actual Kolmogorov distribution, the images are smaller and more numerous than are observed. The spectra also do not exhibit the observed irregularities. Velocity distributions that are somewhat steeper than the Kolmogorov power law lead to calculated images and spectra that reproduce characteristic features of the observations.

Subject headings: masers — turbulence

1. INTRODUCTION

A clumpy structure is often indicated by irregularities in the profiles as well as by the images for spectral line emission from molecular clouds and similar environments. Evidence also exists for turbulence or waves in these regions. It is natural to imagine that these may be related. Because of their characteristic "exponential amplification," astrophysical masers are especially sensitive to variations within the medium, including the coherence of velocities along the lines of sight. Observations of astrophysical masers frequently indicate an extremely clumpy structure, as would be expected. Correlations in the velocities of maser features have been interpreted in terms of turbulence in the masing cloud (Walker 1984; Gwinn 1994). A limited effort has been made to understand the clumpy structure of circumstellar OH masers using a small number of sinusoidal waves (Deguchi 1982).

In the investigation here, we further examine the possibility that clumpiness in maser radiation can be understood in terms of turbulence. Turbulent-velocity fields are created by statistical sampling from Kolmogorov-like distributions for the velocities. The calculational methods are similar to those employed in our study of turbulence in a masing accretion disk (Wallin, Watson, & Wyld 1998). For simplicity, we assume that the medium is uniform except in velocity and that the masers are unsaturated. A detailed comparison is made with observational data about the 25 GHz methanol masers in OMC-1, for which there is reason to believe that these simplifications can be an adequate description.

The calculational methods for creating the turbulent-velocity fields and for finding the emergent intensities as a function of Doppler velocity and location on the surface of the masing volume are presented in § 2. Observational data about the 25 GHz methanol masers are then summarized (§ 3). Observational properties, which are compared with the calculations to constrain and to infer information about the uncertain parameters (§ 4), include the overall width and irregularity in the spectral distribution of the radiation from the entire cloud of masing features, the number and sizes of masing features, and the amplification factor for the strongest masing feature.

2. BASIC CONSIDERATIONS

2.1. *Description of the Turbulent Velocities*

The quantitative description of the methods for creating the turbulent-velocity field have been presented in detail elsewhere (Wallin et al. 1998) and are essentially the same used recently by Dubinski, Narayan, & Phillips (1995) in the context of turbulence in molecular clouds. Kolmogorov-like forms for the power spectra are utilized to describe the velocities. As in the previous investigations, we make the simplification that the turbulent velocity $\boldsymbol{v}_t$ can be obtained from a vector potential $\boldsymbol{A}$, which is strictly valid only for an incompressible medium, $\boldsymbol{v}_t = \nabla \times \boldsymbol{A}$. The mean square of the Fourier component of $\boldsymbol{A}$ for wavenumber $\boldsymbol{k}$ is then

$$\langle |\boldsymbol{A}_{\boldsymbol{k}}|^2 \rangle \propto (k^2 + k_{\min}^2)^{-17/6 - b_e}\,, \tag{1}$$

where $b_e = 0$ gives the Kolmogorov distribution. Here, $k_{\min}$ is introduced to prevent divergence at $k = 0$. As standard approximations, the probability distributions for the $\boldsymbol{A}_{\boldsymbol{k}}$ are taken to be Gaussian. To select a representative velocity field from the statistically allowed possibilities (a "realization"), the $\boldsymbol{A}_{\boldsymbol{k}}$ are obtained by sampling from the Gaussian distribution, utilizing a random number generator. Fast Fourier transform methods are then utilized to create the velocity field from its Fourier components, $\boldsymbol{v}_k = i\boldsymbol{k} \times \boldsymbol{A}_{\boldsymbol{k}}$, in a rectangular volume that contains $256 \times 256 \times 64$ grid points. That this number of grid points is appropriate will be discussed subsequently. The range of wavenumbers that are included for each Cartesian direction is

$$-\frac{1}{2}\frac{2\pi}{L_p} N_p^{\max} \le k_p \le \frac{1}{2}\frac{2\pi}{L_p} N_p^{\max}\,, \tag{2}$$

[1] Astronomical Observatory, Ural State University, Lenin Street 51, Ekaterinburg 620083, Russia.
[2] Department of Physics, University of Illinois, 1110 West Green Street, Urbana, IL 61801.

where $N_p^{\max}$ is 256 or 64, and the corresponding L_p is 4 or 1 for direction p ($=x$, y, or z). The foregoing defines the $\boldsymbol{A}_k$ to within a constant that is adjusted so that the projection of the turbulent velocities along the line of sight has the desired rms value σ_t for the entire volume.

The calculation of the radiation depends only upon the component of the velocity along the line of sight, which we will designate simply as v_t in the remainder of this paper.

2.2. *Formation of Spectral Lines*

Consider now the formation of spectral line radiation for masers in the presence of combined turbulent and thermal velocities. The observed frequency ν and the rest frequency ν_0 are related to the velocity v of the molecule projected along the line of sight, according to the Doppler relationship

$$v = c(\nu_0 - \nu)/\nu_0 \,. \tag{3}$$

The distant observer is located along a line of sight that is considered to be parallel to the x-axis. Since the maser is being treated as unsaturated, the intensity of the radiation that emerges toward the observer from a (y, z) location is determined from the optical depth $\tau(v, y, z)$ for a ray through the slab at fixed (y, z) and with frequency expressed in terms of the Doppler velocity v. For simplicity, we adopt the convention throughout this paper that the optical depth for masing is positive. If N_x grid points ($N_x = 256$ in most of the computations here) are used along the x-axis in the computation, then τ can be expressed as

$$\tau(v, y, z) = \left(\frac{\tau_0}{N_x}\right) \sum_i \exp\left[\frac{-(v - v_t^i)^2}{v_{\rm th}^2}\right] \equiv \tau_0 f(v, y, z) \,, \tag{4}$$

where the sum is over the i locations in x (the grid points) along the path of the ray at which the turbulent velocity is determined, as described in § 2.1. Both the thermal dispersion in velocities $v_{\rm th}$ and the excitation are taken to be constant throughout the slab. Thus, τ_0 would be the optical depth through the slab at the center of the spectral line ($v = 0$) when there is no turbulence ($v_t = 0$). In the presence of significant turbulence, the profile factor $f(v, y, z)$ tends to be irregular and may have several peaks. We designate the $f(v, y, z)$ for the most prominent of these peaks at each (y, z) as $f_m(y, z)$ and the velocity at which it is realized as $v_m(y, z)$. It is convenient to describe the overall characteristics of the maser slab by the value of the largest $f_m(y, z)$ on the surface of the slab, $f_{\max} = \max [f_m(y, z)]$.

Values for v_t^i and for the relative contribution to $\tau(v, y, z)$ are presented in Figure 1 as a function of distance along the paths of representative rays. How the $\tau(v, y, z)$ accumulates in the sum in equation (4) is thus indicated in Figure 1, as well as how this variation depends upon the power spectrum of the velocities. A qualitative change is evident in Figure 1 as b_e increases from zero (Kolmogorov). This reflects the decrease in the contribution of large-k (short-wavelength) components, which cause more rapid spatial variations, as the power spectrum becomes steeper. Additional illustrations of the variation of $f_{\max}$ and $f_m(y, z)$ with the relevant parameters (b_e and σ_t) are given in Table 1. The significant contributions to τ that occur here form well-separated locations and are examples of "aligned masers" (Deguchi & Watson 1989).

As would be expected, an increase in σ_t leads to a decrease in $f_{\max}$ and to an increase in $f_{\max}/f_{\min}$. With the same optical depth along the brightest ray, the surface brightness computed with the higher σ_t is clumpier. For equal values of τ_0, clumps created in a realization with higher σ_t tend to be less pronounced. The observed peak intensity at location (y, z), expressed as a brightness temperature T_m, depends upon f_m, according to

$$T_m(y, z) = T_{\rm bg} \exp\left[\tau_0 f_m(y, z)\right] \tag{5}$$

in the unsaturated limit for a background radiation temperature $T_{\rm bg}$ when spontaneous emission is ignored, as we assume here. Significant variation in f_m with location (y, z) leads to a clumpy appearance in a map of the surface of the rectangular slab. In addition, the v_m can also vary appreciably with location (y, z) so that the peak of the maser line occurs at different velocities in different clumps. Thus the map of maser line emission created in a turbulent medium

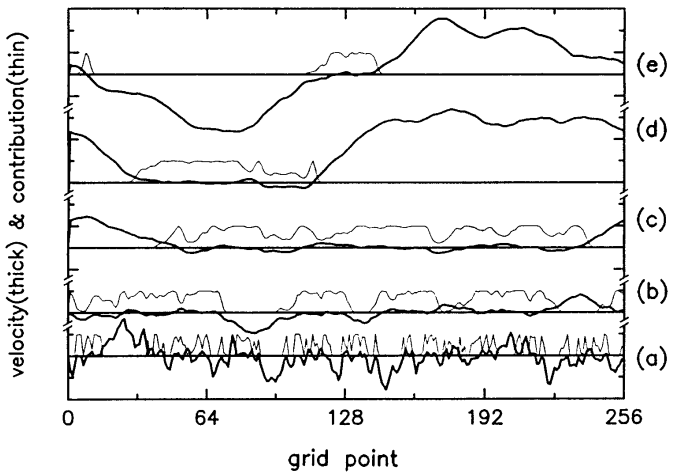

FIG. 1.—Examples of the variation of the Doppler velocity and the factor $\exp[-(v_m - v_t^i)^2/v_{\rm th}^2]$ in the sum for the optical depth $\tau(v, y, z)$ (see eq. [4]) as a function of distance (expressed in terms of grid points) along rays of maser radiation. In each example, the Doppler velocity is plotted relative to the peak velocity v_m for the particular path (v_m is represented by the horizontal line). For the velocity, the distance between marks corresponds to $5v_{\rm th}$, whereas it corresponds to 1 for the factor $\exp[-(v_m - v_t^i)^2/v_{\rm th}^2]$. Curves *a* correspond to the direction toward the brightest point of the map ($b_e = 0$, seed = A), shown in Fig. 3. Curves *b* correspond to the direction toward the brightest point of the map ($b_e = 0.16667$, seed = B) in Fig. 3. Curves *c*–*e* correspond to directions toward the brightest point, the point with average f_m, and the weakest point of the map ($b_e = 1.0$, seed = B) in Fig. 3, respectively.

TABLE 1

SELECTED RESULTS OF COMPUTATIONS FOR THE OPTICAL DEPTHS OF MASING FEATURES IN A TURBULENT SLAB

b_e	Seed	$\sigma_t/v_{\rm th}$	$f_{\max}$	$\tau_{0,\min}$	$\tau_{0,\max}$
0	B	1.53	0.69	...	...
0	B	9.71	0.20	56	76
0	B	4.85	0.35	31	43
0	A	5.02	0.34	30	42
0	C	4.93	0.34	35	45
0.16667.....	B	4.67	0.40	25	35
0.16667.....	A	4.94	0.38	28	40
0.16667.....	D	4.96	0.39	26	36
0.33333.....	B	4.72	0.46	22	31
0.33333.....	A	5.12	0.42	25	35
0.66667.....	B	4.59	0.57	16	23
0.66667.....	A	5.14	0.56	17.5	25
1	B	5.09	0.58	17	25
1	A	5.00	0.59	16	24

NOTE.—See text for definition of parameters. "Seed" is the initial random number used in the generation of velocity field.

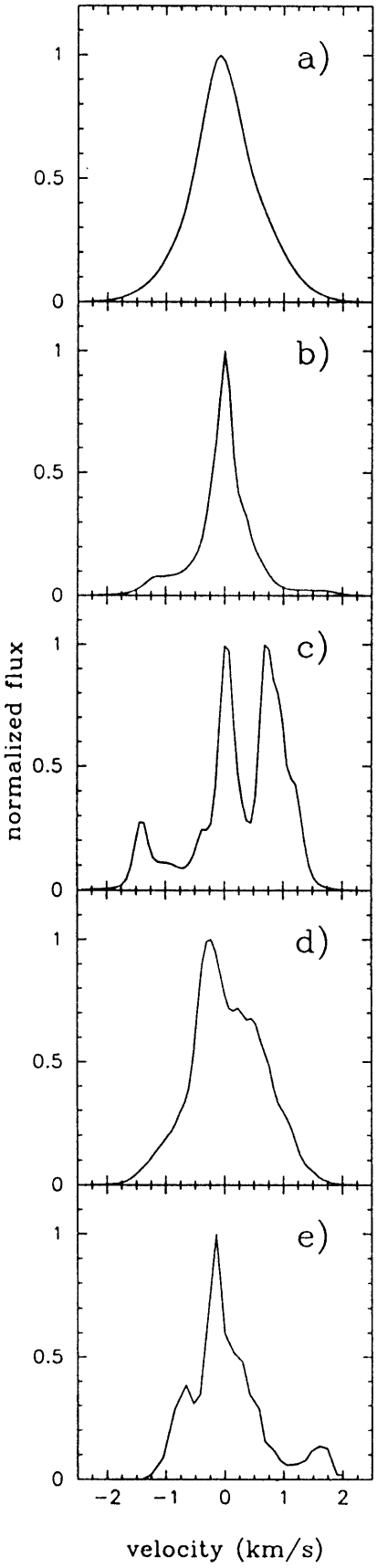

FIG. 2.—Integrated spectral line profiles for the calculations with (*a*) low optical depth, (*b*) a single prominent maser spot, (*c*) multiple prominent maser spots, (*d*) intermediate case, and (*e*) the observed profile from JGSWWM with the central velocity set to zero.

appears as if it is created by a collection of isolated clumps moving with different velocities, even though the physical parameters (except velocity) are constant within the cloud.

Clumps become more pronounced with increasing τ_0, because the differences in the appearance [as measured by $T_m(y, z)$] depend exponentially on the differences in $\tau_0 f_m(y, z)$ among the various locations. An increase in τ_0 also reduces the sizes of clumps for similar reasons. In the limit of very large τ_0, a single peak dominates.

The magnitude of the optical depth can also greatly influence the observed spectral line profiles obtained by integrating $T(v, y, z)$ over y and z. We designate this line profile as the "integrated" line profile. In the optically thin limit, this line profile becomes essentially Gaussian, with a breadth that corresponds to the dispersion in the turbulent velocities [$2(2)^{1/2}\sigma_t$ = full width at e^{-1} of the peak]. Its center is at $v = 0$. With increasing τ_0, the inhomogeneities in the brightness distribution become more prominent, and the integrated spectral line profile deviates from a Gaussian. Asymmetries and spikes can appear. In the limiting case of very large τ_0, the profile consists of a single spike at the v_m associated with the $f_{\max}$. The breadth of this spike is less than that of the thermal velocity dispersion and would be determined by the effects of saturation (which are not being considered in the calculations here).

The sizes and distribution of maser features on the map of the surface of the slab depend on the steepness of the power spectrum of the velocities, as is evident in Figure 2. Just as occurs along the paths of the rays in Figure 1, the turbulent velocities change more rapidly in directions y and z, as well as when the power spectrum (eq. [1]) becomes less steep. As a result, the clumps on the map become smaller and more numerous. The integrated line profile exhibits more spikes.

3. 25 GHz METHANOL MASERS

The 25 GHz methanol masers were first detected by Barrett, Schwartz, & Waters (1971). They can be considered as intense, interstellar, molecular masers since the brightness temperatures of the strongest 25 GHz maser spots exceed 2×10^5 K (Johnston et al. 1992, hereafter JGSWWM). These masers are produced in the J_2–J_1 series of transitions of the methanol molecule with E-type symmetry. The values of principal quantum number J for the observed transitions range from 2 to 13 (Wilson et al. 1993). The 25 GHz masers are observed in a number of sources (see, e.g., Menten et al. 1986; Plambeck & Menten 1990; Menten & Batrla 1989). However, they are known to be quite strong only in OMC-1. Methanol maser emission toward OMC-1 in the J_2–J_1 E series reaches its maximum of about 100 Jy at $J = 6$ (Hills, Pankonin, & Landecker 1975). The maximum is not sharp, and emission in the 5_2–5_1 E and 7_2–7_1 E lines have a flux that is comparable to that in 6_2–6_1 E line (Hills et al. 1975; JGSWWM). Single-dish, spectral line profiles of these lines from OMC-1 are similar. Although the early observations indicated the possibility of time variability of 25 GHz masers (Chui et al. 1974; Barrett, Ho, & Martin 1975), no such variability in the single-dish profiles within observational uncertainties was detected in a comprehensive study by Menten et al. (1988b).

Initial interferometric observations by Matsakis et al. (1980) have shown that the methanol masers form a group of spots which are distributed differently from H_2O or OH masers. Further interferometric observations of 25 GHz methanol masers were carried out by JGSWWM with

much higher spatial and frequency resolution. These observations confirmed the general conclusions of Matsakis et al. (1980) and provided observational data that is currently the most refined. Our comparisons with the observations are based mainly on the JGSWWM data. Further details from the JGSWWM study that are relevant to our investigation are described below.

The JGSWWM observations were performed with the VLA[3] in D configuration, which provides a synthesized beam with a size $3''.31 \times 2''.71$ (p.a. 18). The authors obtained a 256×256 pixel map with a pixel size of $1''$. After self-calibration and deconvolution, a spatial resolution of order $1''$ was achieved. The channel separation was 0.15 km s^{-1}.

JGSWWM have detected 15 maser spots with the peak fluxes in the 6_2–6_1 line greater than about 3 Jy and a "confusing background level of emission at the 3 Jy $beam^{-1}$ level." Five maser spots appeared to be spatially resolved. One of these had a total flux higher than 60 Jy. The spectral line profiles of individual maser spots were single peaked with breadths in the range from 0.15 to 0.9 km s^{-1}. Maser spots and the "background emission" were distributed in the crescent-shaped region located close to (but distinct from) the infrared source IRc2 in Orion KL. The region is about $40''$ long and about $10''$ thick. The integrated spectral profiles of the 6_2–6_1 and 5_2–5_1 lines from the region were asymmetric, with the main peak at V_{lsr} of about 7.8 km s^{-1}, a spike at about 7.3 km s^{-1}, a blob at about 8.3 km s^{-1}, and a minor peak at about 9.7 km s^{-1}. Comparisons with the maps of the spectral line emission due to other molecules brought JGSWWM to the conclusion that the 25 GHz methanol masers arise from the high column density gas located very near the interface of the high-velocity outflow from IRc2 and the surrounding dense gas.

According to estimates, this region is likely to have a hydrogen number density greater than 10^6 cm^{-3} and gas temperature in the range from 50 to 140 K (see, e.g., Menten et al. 1988a; Turner 1989; Irvine, Goldsmith, & Hjalmarson 1987; Johansson et al. 1984; Wright, Plambeck, & Wilner 1996). A consideration of the pumping models for J_2–J_1 E methanol masers (Strelnitskii 1981; Sobolev & Strelnitskii 1983; Sobolev 1993; JGSWWM) has shown that they are pumped by a collisional-radiative mechanism (i.e., a collisional source and a radiative sink of energy). This mechanism is not sensitive to the value of kinetic temperature within the quoted range but is rather sensitive to the hydrogen number density, with a strong preference for approximately 10^6 cm^{-3}. Comparing the values of hydrogen number density in the ambient gas and in the maser sources indicates that masing is not a result of density enhancements. Hence, correlation paths in the turbulent medium created by the outflow from IRc2, not actual physical clumps, are the likely cause of the 25 GHz methanol masers in OMC-1.

4. MODEL OF THE 25 GHz MASER SOURCE

4.1. *Basic Description*

When the maser is completely unsaturated, the emission in the maser line itself does not significantly influence the distribution of populations of energy levels. Hence, one can assume that the rates of radiative processes participating in pumping are ultimately determined by escape probabilities in the pumping lines. For the case of the source in OMC-1, these lines are likely to have optical depths of less than a few (Turner 1991; Johansson et al. 1984). These are effectively optically thin for the purposes here, and the escape probability can thus be approximated as constant within the source. Estimates made in JGSWWM show that brightness temperatures of the bulk of 25 GHz maser spots are not high enough to produce saturation. Hence, most of the general characteristics of the 25 GHz methanol masers in OMC-1 should be reproduced adequately with the approximation of unsaturated masing. Further, the collisional-radiative pumping mechanism for 25 GHz methanol masers in OMC-1 discussed in the previous section chooses the regions with similar densities and is independent of the distance to the external sources of infrared radiation. This allows us to consider the pumping rate as being nearly constant within the source.

We adopt the idealization that the source of maser radiation is a rectangular slab seen edge-on, with dimensions of $40'' \times 10''$ projected onto the field of view. The elongation of the source along the line of sight is assumed to be equal to its longer extension in the field of view. Such geometry corresponds to the hypothesis of JGSWWM: that the source of 25 GHz methanol masers in OMC-1 is formed by the shock front moving at right angles to the line of sight. In our coordinate system, the radial direction (line of sight) corresponds to the x coordinate, the direction of the longer extension of the field of view is represented by the y coordinate, and the direction of the shorter extension of the field of view is represented by the z coordinate. The spacing between points on the spatial grid used for the computations is constant, with 256 points in the x and y directions and 64 in the z direction. For a source size of $40'' \times 10''$, the spatial resolution in the computations is approximately 7 times better than the spatial resolution for the JGSWWM observations.

A thermal breadth of 0.22 km s^{-1} is adopted (FWHM). This value corresponds to a thermal breadth of the methanol molecule at a kinetic temperature of 100 K. A velocity resolution of 0.34 thermal breadths is used in the computations. With the adopted value of thermal breadth, this corresponds to a velocity resolution of 0.075 km s^{-1}, which is two times better than in the JGSWWM observations.

4.2. *Integrated Spectral Line Profiles*

As the first step in the comparison with the observations, we calculate the total emission spectrum of the source by integrating the brightness temperature $T(v, y, z)$ over all points in the field of view. Examples are given in Figure 2.

We have examined models obtained with increasingly steep power spectra for the velocities beginning with b_e equal to 0 (Kolmogorov spectrum) and ranging up to b_e equal to 1. Values of the other parameters were chosen in the following manner: With the specified value of b_e, we determined the value of σ_t, for which the extent of the integrated emission spectrum in velocity agrees with the observational data. We have found that the agreement with observations is achieved for a velocity dispersion σ_t that is greater than about 5 thermal breadths. At the same time it was found that in models with higher velocity dispersion, the individual profiles of the stronger maser spots have

[3] The VLA is operated by the National Radio Astronomy Observatory (NRAO), which is a facility of the NSF, operated under cooperative agreement by Associated Universities, Inc.

multiple peaks. This is in conflict with the observational data. Our attention is thus restricted to models in which intrinsic velocity dispersion is about 5 thermal breadths.

We have also used the integrated spectrum for assessing whether the spatial resolution (the grid size) of our calculations is sufficient. For this, we calculate spectra by skipping alternate grid points in all directions (i.e., x, y, and z). If the spectra differ by less than 10% from those computed with velocities at all of the grid points, we regard the spatial resolution as sufficient. That was always the case with the prominent features described in our study.

One can see from Figure 2 that the spectra can be single or multiple peaked. Some have characteristic features resembling that of the profile obtained by JGSWWM. If the value of τ_0 is low, the spectrum is very close to Gaussian (see Fig. 2*a*). This can be considered as evidence that our calculational scheme works properly, since the random velocity field should produce a Gaussian profile in the optically thin limit. When τ_0 increases, the relative contribution of the more prominent peaks increases. The integrated spectrum deviates from a Gaussian (Figs. 2*b* and 2*d*), and multiple peaks appear in the case when some of the brightest maser spots have comparable fluxes (Fig. 2*c*). Quite often the spectrum has two prominent peaks and thus resembles the spectrum of a source with internal rotation. With increasing τ_0, the peaks of the spectrum also become narrower because of the increasing importance of the brightest points.

Among the characteristics of the masers which could be determined from our calculations are the values of optical depth toward prominent maser spots. In order to delineate these, subject to the specified value of σ_t, we have searched for the range of τ_0 in which the ratio $T_{\max}/T_{\rm bg} = \exp(\tau_0 f_{\max})$ varies from 4000 to 150,000. Here $T_{\max}$ is the antenna temperature of the strongest maser spot for the telescope with 1.″1 beam (spatial resolution of JGSWWM data) and is a characteristic of the model. JGSWWM have found that the brightness temperature of the strongest 25 GHz methanol maser spot in OMC-1 is 2×10^5 K when integrated over a 1.″1 beam. With this value of $T_{\max}$, the above range of $T_{\max}/T_{\rm bg}$ corresponds to values of $T_{\rm bg}$ from 1.3 to 50 K. These $T_{\rm bg}$ values cover the range of likely brightness temperatures for the background emission being amplified by the 25 GHz methanol masers in OMC-1. In Table 1, the ranges of τ_0 (i.e., $\tau_{0,\min} < \tau_0 < \tau_{0,\max}$) are given, within which $T_{\max}/T_{\rm bg}$ varies from 4000 to 150,000. As can be seen from the values of f_m, the optical depth of the maser line toward the strongest maser spot is then in the range from 9 to 15.

The appearance of the spectrum for a particular calculation is determined by the random numbers that are the basis for the particular realization of the velocity field. The number of possibilities is enormous. It is impossible to examine all of the possibilities and to search for the realization that displays the best agreement with observations. We have instead considered a total of about 40 different realizations of the random turbulent-velocity field. Results of our calculations for representative realizations are given in the left-hand panels of Figures 4–7.

We have chosen two sets of realizations for presentation here. Turbulent-velocity fields within each particular set were produced with the same value for the initial number given to the random number generator. Within either of the two sets (designated by their seed numbers "A" and "B"), the smoothed velocity patterns show similarities. These choices allow us to explore the two important cases: when the spectrum is determined by multiple maser spots and when it is determined by a single, prominent maser spot.

Although seed A leads to maps with several prominent maser spots, for $b_e < 0.17$ their integrated spectra exhibit only one broad peak when the values of τ_0 are compatible with the requirement that $T_{\max}/T_{\rm bg} < 150,000$. Integrated spectra from calculations with higher values of b_e, shown in the left panels of Figures 4 and 5, display asymmetry and spikes, which are characteristic features of the observed single-dish profiles of 6_2–6_1 and 5_2–5_1 lines from OMC-1. In this sense, our calculations are in agreement with observations when b_e exceeds 0.17. It should be noted that the calculations with higher values of optical depth toward the strongest maser spot ($f_{\max}\tau_0 > 12$) reproduce the observed spectra better.

Spectra displayed in Figures 6 and 7 based on seed B (one dominant maser spot) exhibit a single peak in the integrated emission spectrum. The breadth of this peak is in agreement with that of the main peak of the observed spectrum when the value of b_e exceeds 0.17. Spectra of this set do not directly reproduce the characteristic features of the observed profile. However, consideration of these is relevant because sources of 25 GHz methanol maser emission might consist of several independent slabs.

4.3. *Maps of Peak Brightness Temperature*

The second step in comparing the calculations with observational data consists of producing maps for the peak values of maser line emission. That is, $T_m(y, z)$ from equation (5) is plotted versus y and z.

Maps with different values of b_e for two sets of calculations (multiple and single prominent maser spots) are shown in Figure 3. The optical depths τ_0 for the models correspond to the case when the ratio $T_{\max}/T_{\rm bg}$ is 150,000. It is clearly seen that the maps for lower values of b_e (i.e., when the spectrum of turbulent velocities is less steep) contain more numerous features with smaller sizes. This reflects the fact that the distribution of the turbulent velocities is less smooth when the spectrum of velocities is flatter and the components at large k are more important. It should be noted that the size of the bulk of maser spots tends to be determined by the value of b_e, while the number of maser spots depends greatly on the particular realization of the turbulent-velocity field. There are fewer features in the maps that correspond to values of $b_e \gtrsim 0.666$ than the number of 25 GHz maser spots observed by JGSWWM. This constrains the steepness of the turbulent spectrum in the part of OMC-1 that is being considered. That is, if the maser source represents a single slab, then the b_e value in it should not exceed 0.666.

To compare our calculated maps with the observational data, we have smoothed our maps with a 1.″1 beam. The resulting maps are shown in the central panels of Figures 4–7. In the maps which are obtained with lower values of τ_0 (i.e., when the ratio $T_{\max}/T_{\rm bg}$ is equal to 4000; see Figs. 4 and 6), the features have sizes which are substantially larger than the observational sizes. Most of the features are merged. This also is in conflict with the observational data.

In Figures 5 and 7, we demonstrate that general agreement between the appearance of the calculated map and that of OMC-1 in the 25 GHz methanol maser line is obtained when the optical depth τ_0 in the calculations is

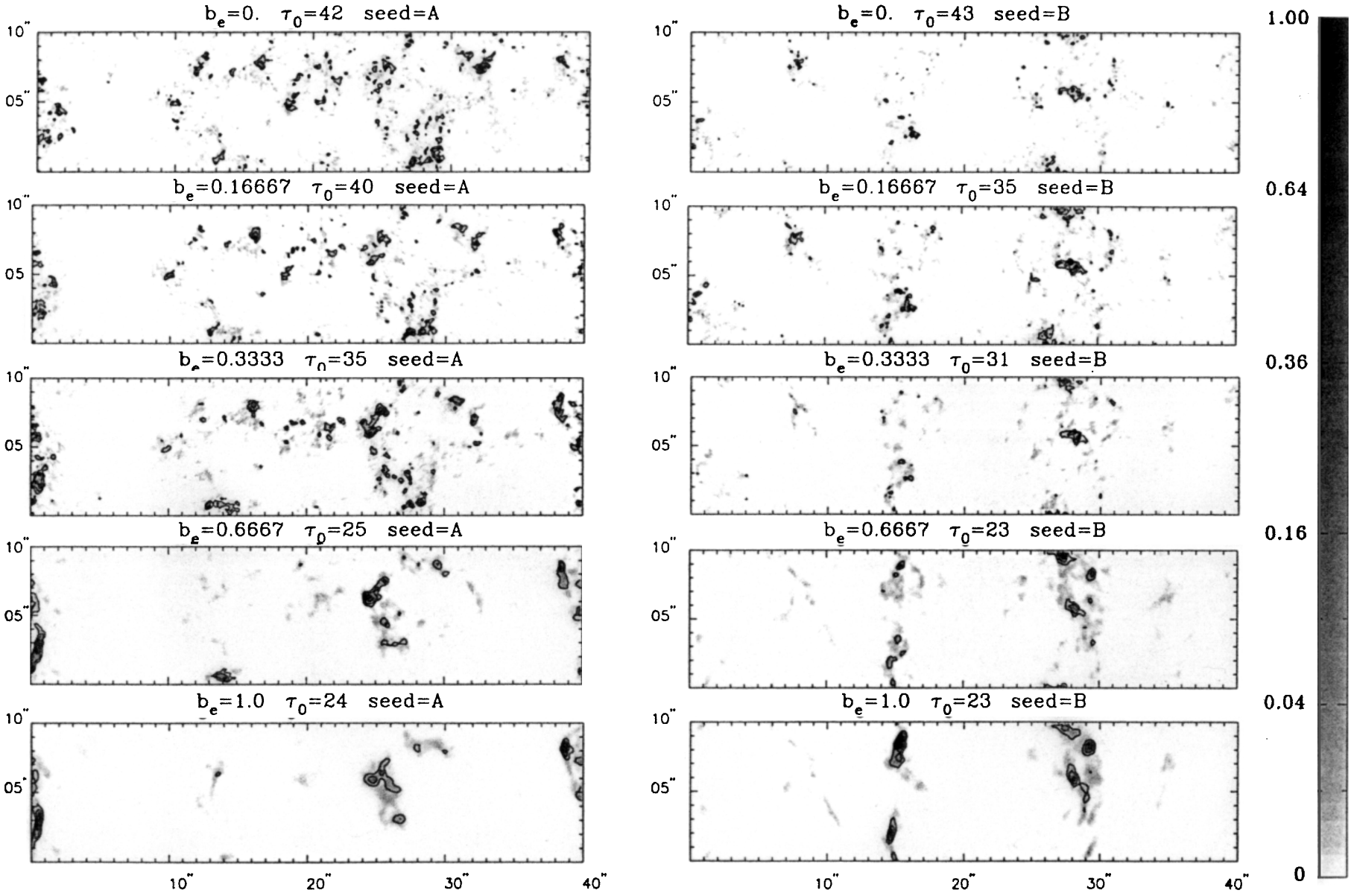

FIG. 3.—Unfiltered maps for models when the brightness of the strongest pixel is about $1.5 \times 10^5 T_{bg}$. Contours correspond to 0.03, 0.10, and 0.30 of the peak brightness.

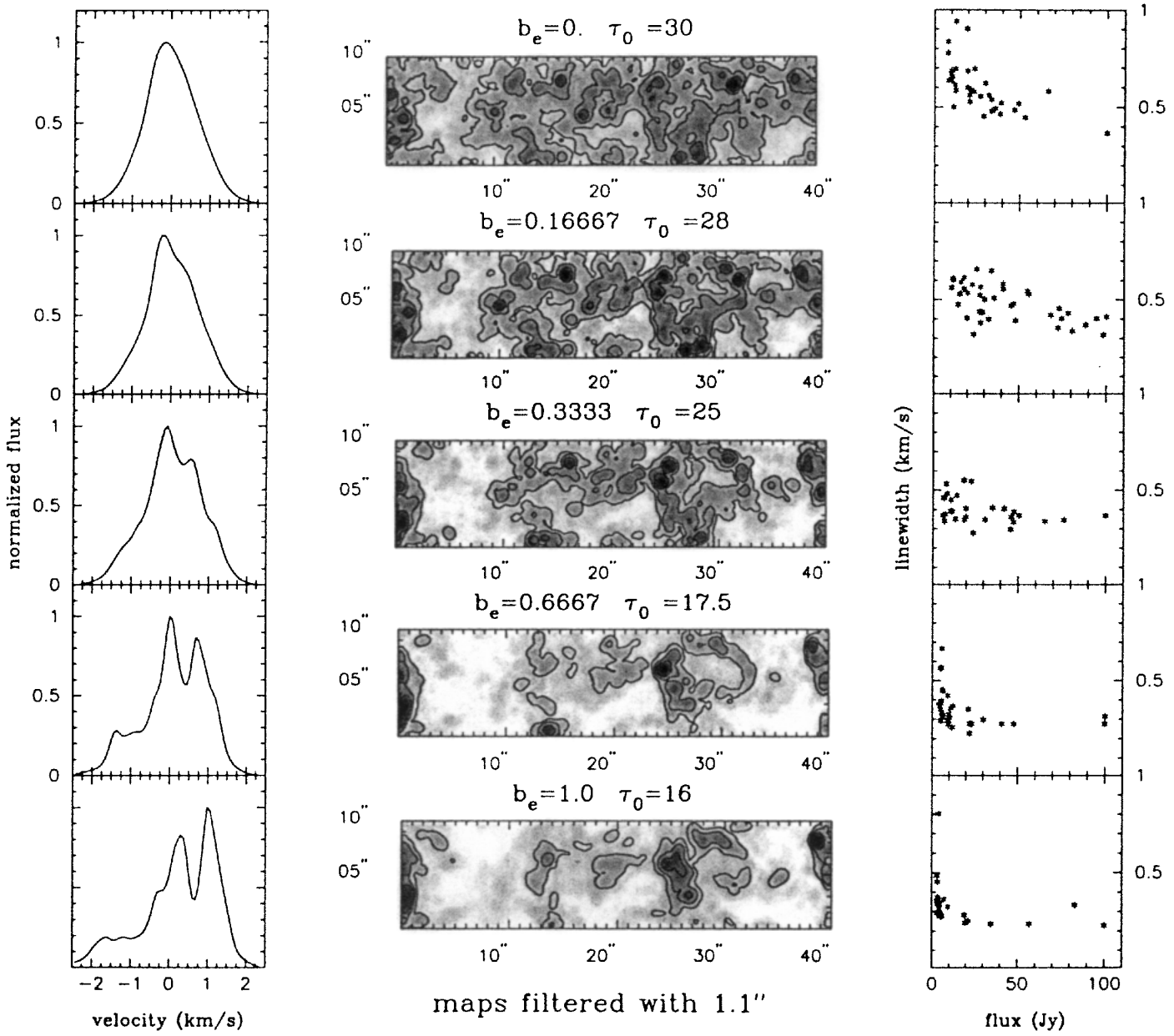

FIG. 4.—Integrated spectral line profiles (*left panels*), maps filtered with 1.″1 beam (*central panels*), and line width vs. flux for the spots shown in maps (*right panels*). These models have multiple prominent maser spots, and the antenna temperature of the brightest spot is $4 \times 10^3 T_{bg}$. Gray scale and contours have the same meaning as in Fig. 3.

increased to $\tau_{0,max}$ (i.e., when the ratio T_{max}/T_{bg} is equal to 150,000). Indeed, maps of the calculated $T_m(y, z)$ look like collections of observed maser spots, mainly unresolved with 1.″1 beam. Some of the spots are merged and formed into elongated features. The number of spots is about the observed number for the calculations, with b_e less than 0.666. Except for the prominent maser spots, a randomly organized background at a flux level of about 0.03 of the peak value is present in the map (the presence of a background at this level was reported by JGSWWM).

4.4. *Relationship between Spectral Line Breadth and Brightness for Maser Spots*

As a further step in comparing the calculations with the data, we have placed the prominent maser spots in "flux–line width" diagrams. These diagrams are shown in the right-hand panels of Figures 4–7. The line widths are the FWHMs of line profiles calculated toward the brightest point of the spot. The fluxes are normalized to facilitate a direct comparison with observations. The value of the flux toward the strongest maser spot was assumed to be 100 Jy, which is close to the observed flux. The diagrams show that the spread in the line widths at a specific value for the flux decreases with increasing flux. This agrees with observational data. In all of the calculations that we have examined, the spectral lines from the brightest spots are rather narrow (0.2–0.4 km s^{-1}). This does not agree with the observational data for which the line width of the brightest spot is about 0.6 km s^{-1}.

A detailed examination of this discrepancy is beyond the scope of our paper. However, the most natural explanation is in the simplicity of our idealization, most likely in the assumption of completely unsaturated masing. According to estimates given in JGSWWM, emission from the strong-

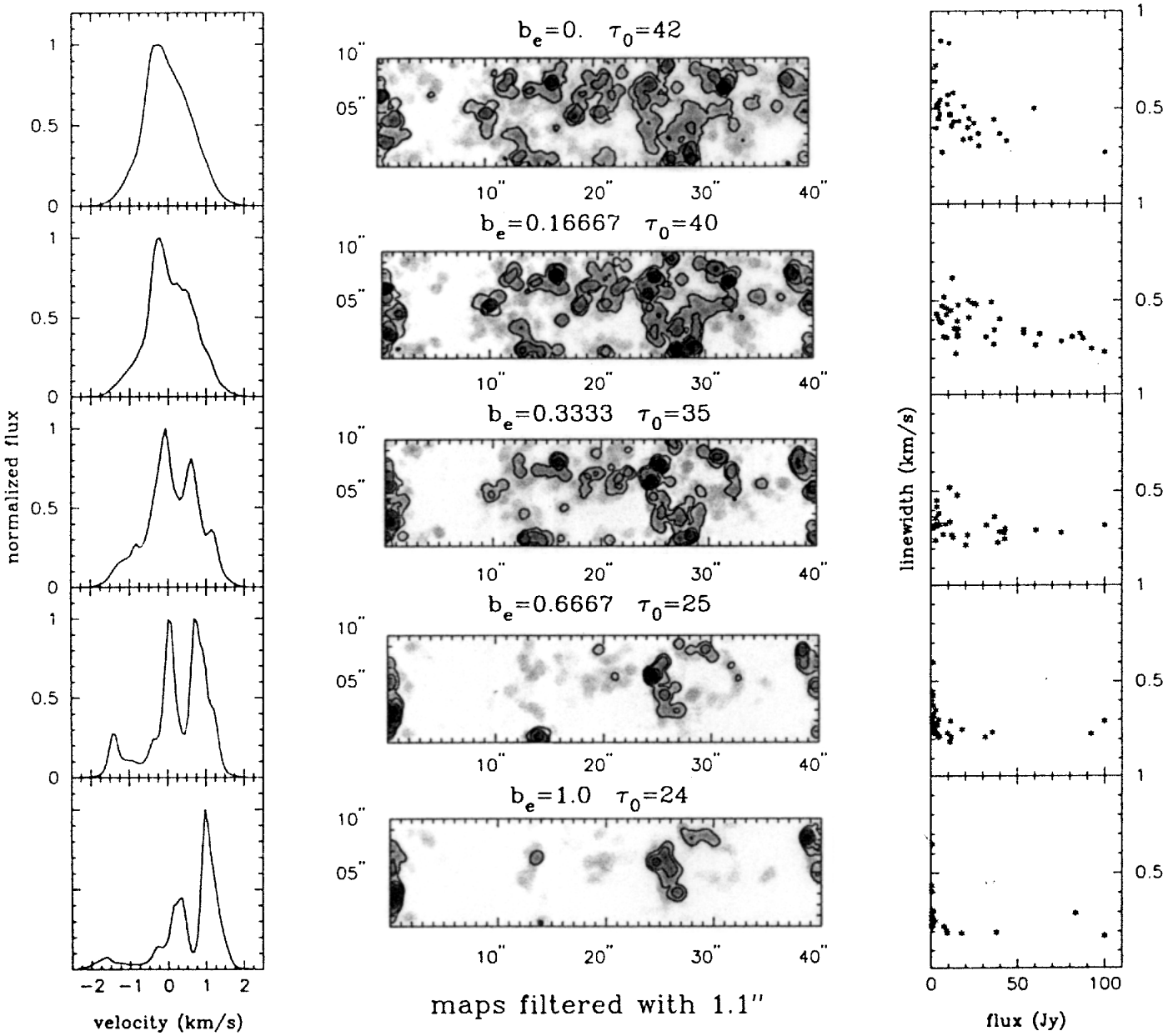

FIG. 5.—Same meaning as Fig. 4, except that the antenna temperature of the brightest spot is to $1.5 \times 10^5 T_{bg}$. These models also have multiple prominent maser spots.

est spots should reflect somewhat the effects of saturation. From § 4.2, the maser amplification of the background radiation is likely to be a factor of approximately 10^5 for these spots. Hence, their optical depth is about 12. When saturation of the maser is completely ignored (as is done in our calculations), the calculated spectral line breadth tends to be narrower by a factor (optical depth)$^{1/2} \simeq 3.4$ than the line breadth of a fully saturated linear maser. Although this factor is strictly valid only for a masing medium with a linear geometry in which the velocity dispersion can be characterized by a single Gaussian, it should be an adequate guide to conclude that (if properly treated) the effects of saturation can plausibly cause a factor of 2 increase in the line breadths of the brightest maser spots. Introducing such a factor in our diagrams leads to good agreement with the observational data. A full calculation of the effects of saturation in an inhomogeneous, three-dimensional medium would represent a considerable advance over the current calculation and over calculations in the literature.

5. CONCLUSIONS

The basic features of the 25 GHz methanol masers in OMC-1—the images and the integrated spectral line profile—are generally compatible with the results of calculations for maser emission from a turbulent slab of gas. Together with similar conclusions about the water masers in a circumnuclear accretion disk (Wallin et al. 1998), this suggests that velocity fields alone can be the cause for much of the clumpy appearance of astrophysical masers and, perhaps, of spectral line emission from molecular environments in astrophysics in general. Independent evidence exists for turbulence, or at least for collections of waves that would be expected to have a similar influence on the radiative transport. A significant role for variations in other relevant properties (e.g., excitation, temperature, density, or chemical composition) cannot, however, be excluded. It is

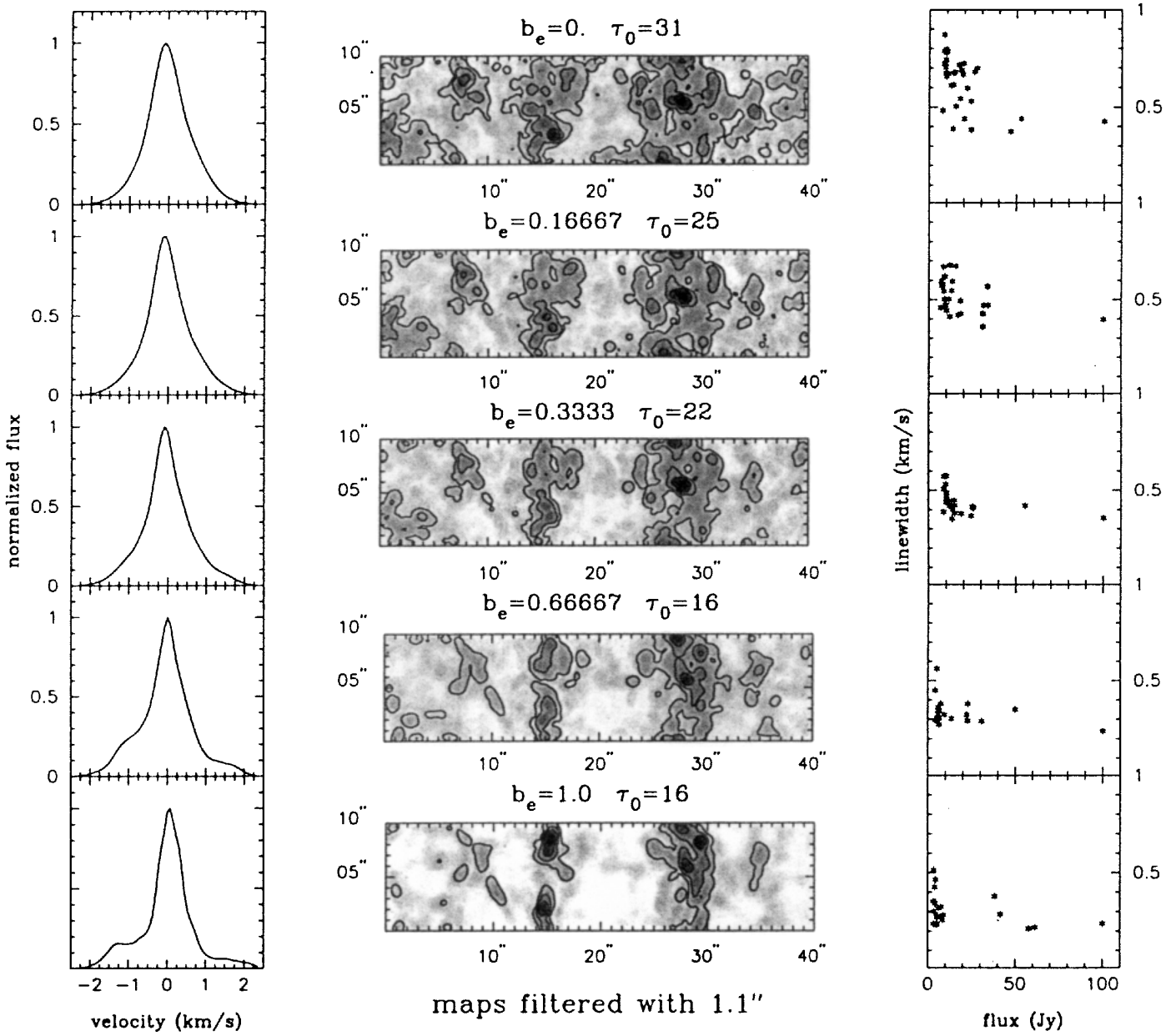

FIG. 6.—Same meaning as Fig. 4, except that these models have a single prominent maser spot. The antenna temperature of the brightest spot corresponds to $4 \times 10^3 T_{bg}$.

likely that the chief deficiency in our calculations for the 25 GHz methanol masers—insufficient breadth for the spectral lines from the more intense, individual masing features—is a result of our simplification to completely unsaturated masing. Effects of saturation will broaden the spectral lines.

Comparisons between the observations and the calculations do restrict the parameters that describe the 25 GHz methanol masing in OMC-1. The velocity dispersion for the turbulence is about 1 km s^{-1} (rms), and the magnitude of the optical depth is about 12–15. The slab of masing gas is considered to be in the region of interaction between the outflow from the young stellar object and the ambient medium and is to be viewed edge-on. When viewed from other angles, the maser radiation would thus be much less intense. This would be consistent with the observation that bright 25 GHz methanol masers are rare. The remaining parameter in the calculations, in addition to the rms turbulent velocity σ_t and the optical depth τ_0, measures the dependence of the spectral distribution for the velocities on the wavenumber k and is expressed as b_e in equation (1). The requirement that the spectrum of maser radiation integrated over the surface of the masing cloud exhibit significant deviations from a smooth Gaussian stipulates that $b_e > 0.17$, and hence that $\langle |v_k^2| \rangle$ decrease faster than Kolmogorov, with increasing wavenumber, by at least a factor of $k^{1/3}$. In contrast, the number of masing features on the surface of the slab will be too few unless $b_e < 0.67$. Thus, the ratio of the inferred $\langle |v_k^2| \rangle$ from the calculations to that for Kolmogorov distribution is between $k^{-1/3}$ to $k^{-4/3}$.

We are grateful to H. W. Wyld for helpful discussions during the course of this investigation, as well as to E. C. Sutton for helpful comments on the manuscript. Support from NSF grant AST94-01348 is acknowledged, as is support for B. K. W. through a GSRP fellowship from NASA.

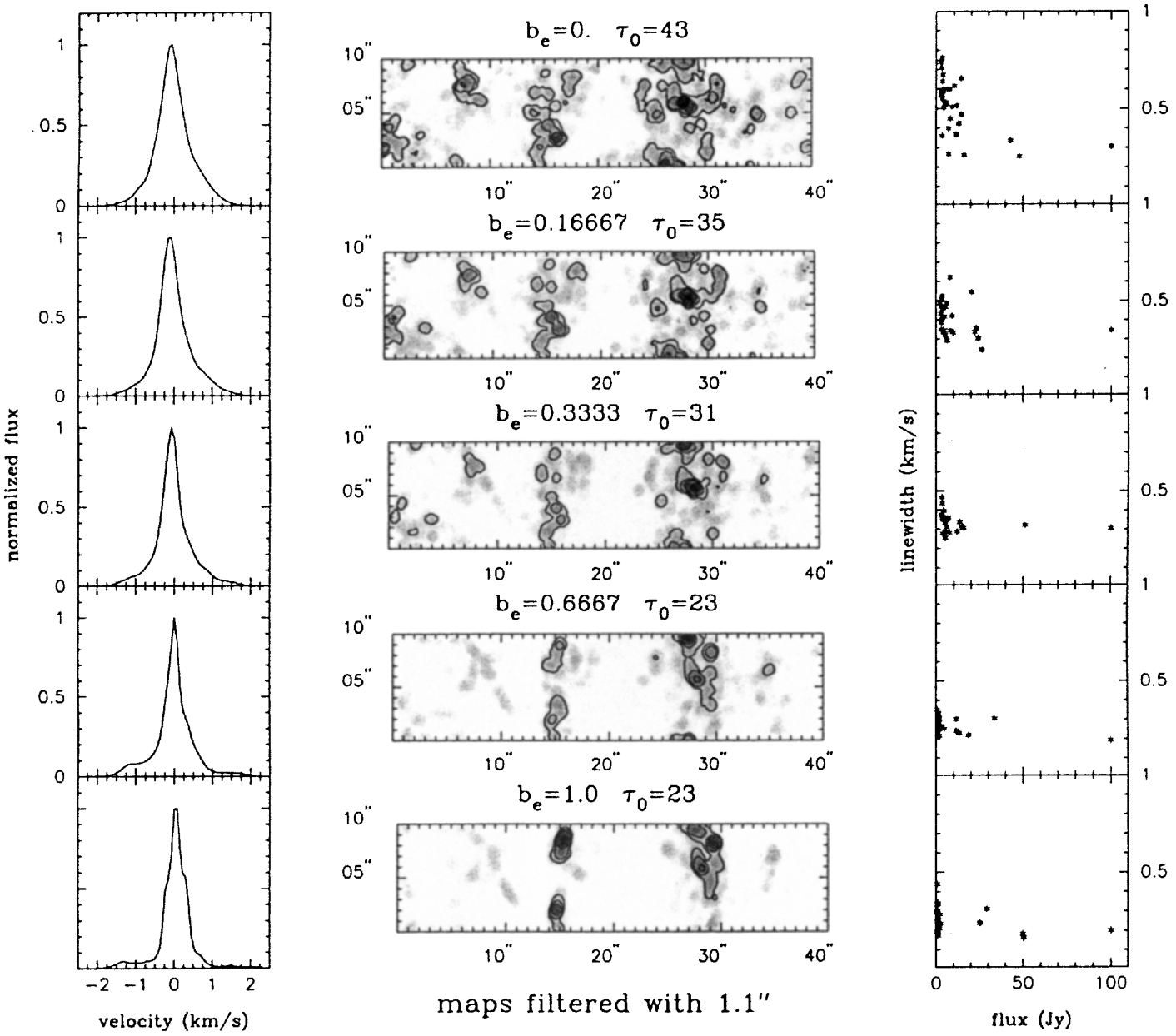

FIG. 7.—Same meaning as Fig. 4, except that these models have a single prominent maser spot, and the antenna temperature of the brightest spot is $1.5 \times 10^5 T_{bg}$.

REFERENCES

Barrett, A. H., Ho, P., & Martin, R. N. 1975, ApJ, 198, L119
Barrett, A. H., Schwartz, P. R., & Waters, J. W. 1971, ApJ, 168, L101
Chui, M. F., Cheung, A. C., Matsakis, D., Townes, C. H., & Cardiasmenos, A. G. 1974, ApJ, 187, L19
Deguchi, S. 1982, ApJ, 259, 634
Deguchi, S., & Watson, W. D. 1989, ApJ, 340, L17
Dubinski, J., Narayan, R., & Phillips, T. G. 1995, ApJ, 448, 226
Gwinn, C. R. 1994, ApJ, 429, 241
Hills, R., Pankonin, V., & Landecker, T. L. 1975, A&A, 39, L149
Johansson, L. E. B., et al. 1984, A&A, 130, 227
Johnston, K. J., Gaume, R., Stolovy, S., Wilson, T. L., Walmsley, C. M., & Menten, K. M. 1992, ApJ, 385, 232
Matsakis, D. N., Cheung, A. C., Wright, M. C. H., Askne, J. I. H., Townes, C. H., & Welch, W. J. 1980, ApJ, 169, 271
Menten, K. M., & Batrla, W. 1989, ApJ, 341, 839
Menten, K. M., Walmsley, C. M., Henkel, C., & Wilson, T. L. 1986, A&A, 157, 318
Menten, K. M., Walmsley, C. M., Henkel, C., & Wilson, T. L. 1988a, A&A, 198, 253
———. 1988b, A&A, 198, 267
Nedoluha, G. E., & Watson, W. D. 1991, ApJ, 367, L63
Plambeck, R. L., & Menten, K. M. 1990, ApJ, 364, 555
Sobolev, A. M. 1993, in Lecture Notes in Physics 412, Astrophysical Masers, ed. A. W. Clegg & G. E. Nedoluha (Berlin: Springer), 215
Sobolev, A. M., & Strelnitskii, V. S. 1983, Soviet Astron. Lett., 9, 12
Strelnitskii, V. S. 1981, Soviet Astron. Lett., 7, 223
Turner, B. E. 1989, Space Sci. Rev., 51, 235
———. 1991, ApJS, 76, 617
Walker, R. C. 1984, ApJ, 280, 618
Wallin, B. K., Watson, W. D., & Wyld, H. W. 1998, ApJ, 495, 774
Wilson, T. L., Huettemeister, S., Dahmen, G., & Henkel, C. 1993, A&A, 268, 249
Wright, M. C. H., Plambeck, R. L., & Wilner, D. J. 1996, ApJ, 469, 216